Nanoengineered Polypyrrole-Coated Fe_2O_3@C Multifunctional Composites with an Improved Cycle Stability as Lithium-Ion Anodes

*Fei Han, Duo Li, Wen-Cui Li, Cheng Lei, Qiang Sun, and An-Hui Lu**

Novel multifunctional composites composed of highly dispersed nanosized Fe_2O_3 particles, a tubular mesoporous carbon host, and a conductive polypyrrole (PPy) sealing layer are hierarchically assembled via two facile processes, including bottom-up introduction of Fe_2O_3 nanoparticles in tubular mesoporous carbons, followed by in situ surface sealing with the PPy coating. Fe_2O_3 particles are well-dispersed within the carbon matrix and PPy is spatially and selectively coated onto the external surface and the pore entrances of the Fe_2O_3@C composite, thereby bridging the composite particles together into a larger unit. As an anode material for Li-ion batteries (LIBs), the PPy-coated Fe_2O_3@C composite exhibits stable cycle performance. Additionally, the PPy-coated Fe_2O_3@C composite also possesses fast electrode reaction kinetics, high Fe_2O_3 use efficiency, and large volumetric capacity. The excellent electrochemical performance is associated with a synergistic effect of the highly porous carbon matrix and the conducting PPy sealing layer. Such multifunctional configuration prevents the aggregation of NPs and maintains the structural integrity of active materials, in addition to effectively enhancing the electronic conductivity and warranting the stability of as-formed solid electrolyte interface (SEI) films. This nanoengineering strategy might open new avenues for the design of other multifunctional composite architectures as electrode materials in order to achieve high-performance LIBs.

1. Introduction

Rechargeable Li-ion batteries (LIBs) that can store sustainable energy have become more and more important in recent years for portable electronic devices and electric vehicles. However, in order to satisfy the demands of these electronic products, it is essential to develop lightweight, nontoxic, durable Li-ion batteries with greater capacity.[1–6] Recently, it has been found that transition metal oxides such as Fe_2O_3,[7] Fe_3O_4,[8] Co_3O_4,[9] and NiO[10] exhibit high reversible capacities, greatly spurring the rapid development of this field. Among these promising anode materials, iron oxide (Fe_2O_3) have been investigated intensively due to its great advantages such as high theoretical capacity of 1007 mA h g^{-1}, natural abundance, low cost, environmental friendliness, and high resistance to corrosion.[11–14] When coupled with its higher inherent densities (5.24 g cm^{-3} vs. 2.16 g cm^{-3} for graphite), Fe_2O_3 offers about six times higher volumetric capacity than graphite, which is another big advantage for smaller battery packs.[15] Unfortunately, despite their numerous advantages, the practical application of Fe_2O_3 as anode for Li-ion batteries is hampered by poor capacity retention because of the drastic volume change (over 200%) that inherently accompanies the conversion reaction processes, resulting in severe pulverization of the particles and loss of electrical connectivity upon electrochemical cycling, especially at high rates.[4,16] In addition, the formation of a thick solid electrolyte interphase (SEI) films on Fe_2O_3 anode surface causes consumption of abundant Li^+ and a large irreversible capacity (i.e., low coulombic efficiency).[17,18] Furthermore, the unstable SEI films formed during Li^+ insertion may decompose completely, catalyzed by transition metals formed during the Li^+ extraction processes, thus leading to repeated formation/decomposition of the SEI films, resulting in capacity fading and safety problems.[19,20] Meanwhile, the damage of surface SEI also origins from the expansion and shrinkage of Fe_2O_3 materials during cycles.[21] Therefore, it still remains a great challenge to fabricate a stable Fe_2O_3 anode over extended cycling with high reversible capacity and excellent rate capability.

One effective approach to alleviate the pulverization of active materials is to pass the Fe_2O_3 from the bulk form to delicate nanostructures with a short lithium diffusion path, large surface area and an enhanced reactivity.[16,22–24] In well-designed nanostructures, not only is the lithium transfer much easier, but also the strain of volume expansion associated with lithium intercalation is often better accommodated, resulting in considerably improved cycle stability.[11,25,26] Nevertheless, the increased interfaces between nanostructures Fe_2O_3 and the electrolyte may raise the risk of side reactions involving repeated formation and/or decomposition of SEI films, causing capacity loss and safety problems.[27] Moreover, the active nanoparticles

F. Han, D. Li, Prof. W.-C. Li, C. Lei, Q. Sun, Prof. A.-H. Lu
State Key Laboratory of Fine Chemicals
School of Chemical Engineering
Faculty of Chemical, Environmental and Biological Science and Technology
Dalian University of Technology
Dalian 116024, P. R. China
E-mail: anhuilu@dlut.edu.cn

DOI: 10.1002/adfm.201202254

(NPs) tend to aggregate into larger and inactive clusters during cycling, and also results in a deterioration of the reversible capacity.[3] Consequently, it is believed that Fe_2O_3 active materials simultaneously possessing both stable nanostructures and low contact interfaces with electrolyte can exhibit excellent cycle stability and durability. Currently fabrication of Fe_2O_3@carbon composites is proposed as an effective technique combining above mentioned structure features to improve the cycle performance of nanostructured electrode materials.[19,28,29] It is noted that the conductive carbon matrix not only improves the electronic conductivity of active materials and prevents the pulverization and aggregation of NPs, but also overcomes the undesirable side reactions between active materials and the electrolyte, due to its intrinsical conductivity and excellent chemical durability; it also has low cost.[30,31] Therefore, extensive research has been focused on developing composite materials with homogeneously encapsulated metal oxides NPs into a carbon matrix for advanced lithium ion anodes.

Nevertheless, the design of carbon-coated Fe_2O_3 composites has rarely been addressed in studies due to the poor thermal stability of Fe_2O_3 nanostructures, since it is easily reduced to Fe^{2+} and/or Fe^0 at 600 °C.[15,18] It is suggested that the selection of a suitable carbon host is of crucial importance for the preparation of high performance Fe_2O_3@C anodes. Very recently, we have demonstrated a facile method to homogeneously encapsulate ultrafine SnO_2 particles into a tubular mesoporous carbon matrix.[32] This tubular nanostructure provides a confined nanospace for hosting immobilized active NPs, compensating for its volume expansion, maintaining a high dispersity of NPs, and warranting efficient contact between NPs and the carbon matrix during charge/discharge processes, so that, the composite exhibits an ultrahigh Li^+ storage capacity and excellent cycle stability. Nevertheless, there is a large contact interface between active materials and electrolyte, which is detrimental for transition metal oxide Fe_2O_3 NPs. Inspired by the aforementioned works, an Fe_2O_3-based anode material with enhanced cycle stability should incorporate these features: high dispersity of active NPs, good electronic conductivity, efficient electrical contact, and stable SEI film on the interface between electrode material and electrolyte. Thus, it is evident that no single material can meet the demand of high-performance LIBs, thus requiring a more sophisticated construction of desired multifunctional composite materials.

Excitingly, electronically conducting polymers with high conductivity, chemical stability, and low cost have been demonstrated as surface coating layer and/or active matrix for application in batteries to enhance the structural stability and cycle performance.[33,34] More importantly, it has been well-accepted that the SEI layer on conducting polymers surface is relative stable.[35,36] In this paper, we deliberately, successfully and hierarchically designed a novel multifunctional composites composed of highly dispersed nanosized Fe_2O_3 particles, a tubular mesoporous carbon host, and conductive PPy according to the different functions of each component, which were engineered for the improvement of the electrochemical performance of Fe_2O_3-based anodes. Among these components, the ultrathin PPy protective layer can avoid direct contact between Fe_2O_3 and solvent and bridge the electronic channel between Fe_2O_3@C particles. Meanwhile, the tubular mesoporous carbon matrix allows Fe_2O_3 NPs with high dispersity and maintains the efficient electrical contact between the active particles and the matrix. Combining such fascinating synergistic effects of ultrathin PPy protective and conductive layer and tubular mesoporous carbon matrix with large pore volume and thin carbon walls ensures that such a hierarchically nanoengineered multifunctional composite is a promising anode material for highly efficient LIBs.

2. Results and Discussion

2.1. Schematic Presentation for the Nanoengineered PPy-Coated Fe_2O_3@C Multifunctional Composites

Tubular mesoporous carbon with high pore volume (2.16 $cm^3\ g^{-1}$) and thin carbon walls (2 nm) was employed as the matrix for the fabrication of the multifunctional composite.[32] As shown in **Scheme 1**, $Fe(NO_3)_3 \cdot 9H_2O$ solution was impregnated into the mesopore channels of the carbon matrix and subsequently converted to Fe_2O_3 after thermal treatment at 400 °C for 4 h in an argon atmosphere. As the tap density and volumetric energy density of Fe_2O_3@C composites depend on the Fe_2O_3 content, a high loading of Fe_2O_3 was achieved via increasing the concentration of $Fe(NO_3)_3 \cdot 9H_2O$ precursor and impregnation times. A part of Fe_2O_3 particles exposed and agglomerated on the external surface of carbon matrix at high Fe_2O_3 loading (greater than 45 wt%). In order to avoid the formation of unstable SEI on exposed areas of Fe_2O_3 and enhance the electronic conductivity of Fe_2O_3@C composites with a high Fe_2O_3 loading, we took inspiration from nature, in particular the structure of the frog eggs, which are coated with a gel-like film (Figure S1, Supporting Information). The presence of

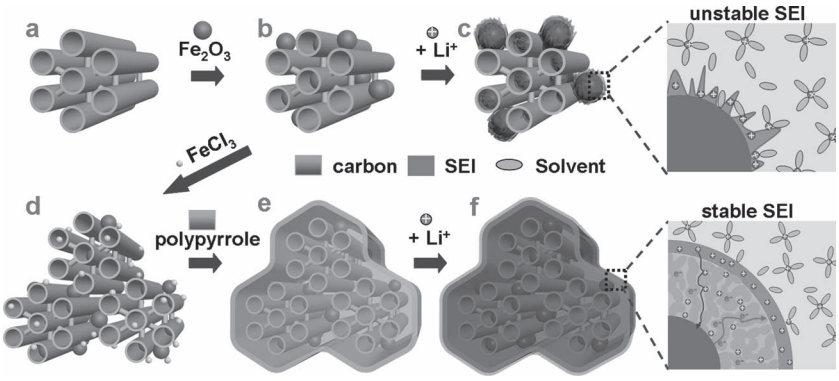

Scheme 1. Illustration of the nanoengineering principles of PPy-coated Fe_2O_3@C multifunctional composites and scheme of enhanced cycle performance: a) tubular mesoporous carbon, b) Fe_2O_3@C composites with high Fe_2O_3 loading, c) unstable SEI film on the surface of Fe_2O_3 NPs during the insertion/extraction of lithium, d) Fe_2O_3@C composites impregnated with $FeCl_3$ oxidant, e) PPy-coated Fe_2O_3@C multifunctional composites, and f) stable SEI film on the surface of PPy during the insertion/extraction of lithium.

the gel-like film is an essential element that acts as a buffer to accommodate mechanical strain, prevents pollution by impurities, and bridges the eggs together to convert a big cluster. The eggs are protected by this gel-like film, which allows them to hatch in safety. Herein, a solution, composed of $FeCl_3 \cdot 6H_2O$ as the oxidant and *p*-toluenesulfonic acid as the dopant, impregnated and deposited onto the external surface and the pore entrances of the Fe_2O_3@C composites, due to the as-prepared Fe_2O_3 particles occupying the carbon channels. Lastly, pyrrole monomer can be spatially and selectively polymerized around the active sites via in situ chemical vapor polymerization at room temperature, leading to the formation of hierarchical PPy-coated Fe_2O_3@C multifunctional composites.

2.2. Properties and Electrochemical Performances of Fe_2O_3@C Composites with Different Fe_2O_3 Loading

The Fe_2O_3 loading of as-prepared Fe_2O_3@C composites can be quantified via TG under air. As shown in **Figure 1**a, all composites display a negligible mass loss below 300 °C, which is generally attributed to the evaporation of adsorbed water. A considerable mass loss corresponding to the removal of carbon species is commonly observed in the temperature region of 300–650 °C for the Fe_2O_3@C composites. As the concentration of $Fe(NO_3)_3$ precursor and impregnation times increase, the mass losses are reduced, suggesting an increased Fe_2O_3 loading in the carbon matrix. From the magnitude of a mass loss, the Fe_2O_3 loadings in these four samples are calculated to be 16 wt% for C-Fe-16, 23 wt% for C-Fe-23, 45 wt% for C-Fe-45, and 50 wt% for C-Fe-50. The measured tap densities of these samples are listed in **Table 1**.

Table 1. Textural parameters of Fe_2O_3@C composites, and PPy-coated Fe_2O_3@C.[a)]

Sample	Fe_2O_3 [wt%]	S_{BET} [$m^2\ g^{-1}$]	V_{total} [$cm^3\ g^{-1}$]	ρ_{tap} [$g\ cm^{-3}$]	D_{size} [nm]	d_{311} [Å]
C-Fe-16	16	869	0.60	0.19	4.5	2.555
C-Fe-23	23	737	0.42	0.39	5.0	2.552
C-Fe-45	45	385	0.20	0.67	8.2	2.536
C-Fe-50	50	303	0.17	0.79	9.1	2.527
C-Fe-50-PPy	47	88	0.08	1.04	—	—

[a)] S_{BET}: BET specific surface area was calculated over the P/P_0 range 0.03 to 0.25; V_{total}: total pore volume at $P/P_0 \approx 0.99$; ρ_{tap}: tap density based on the ratio of the mass and the volume of powders; D_{size}: crystallite sizes were estimated by the Scherrer formula; d_{311}: lattice spacing of (311) plane was obtained by Rietveld refinement with the software MDI Jade 5.0.

Following the TG analysis, the crystallographic structures of the samples were analyzed by wide-angle XRD (Figure 1b). Characteristic diffraction peaks were observed at 30.2°, 35.6°, 43.3°, and 62.9°, which are assigned to the (220), (311), (400), and (440) lattice planes of γ-Fe_2O_3 (maghemite phase; JCPDS card No. 39-1346). This is in agreement with our previous study.[37] As shown in Figure 1b, two very broad and weak diffraction peaks at 35.6° and 62.9° are detected in the samples of C-Fe-16 and C-Fe-23, indicating the existence of extremely small and highly dispersive nanocrystals. In contrast, when increasing the γ-Fe_2O_3 loading, composites C-Fe-40 and C-Fe-50 exhibit relatively narrow and sharp characteristic diffraction peaks of iron oxides, illustrating that the γ-Fe_2O_3 crystallites grow up with an increased loading. The crystallite size was estimated using the Scherrer equation based on the half-width of the (311) reflection and the lattice spacing of (311) plane was obtained by Rietveld refinement with the software MDI Jade 5.0. These results are summarized in Table 1. The calculated crystallite sizes of γ-Fe_2O_3 in C-Fe-16, C-Fe-23, C-Fe-45, and C-Fe-50 are 4.5, 5.0, 8.2, and 9.1 nm, respectively.

The pore structures and the Brunauer-Emmett-Teller (BET) surface areas of the Fe_2O_3@C composites were subsequently determined using N_2 sorption measurement at 77 K. The nitrogen sorption isotherms and Barrett-Joyner-Halenda (BJH) pore size distributions of these samples are compared in Figure 1c and Figure S2 (Supporting Information), and the textural parameters (S_{BET} and V_{total}) are listed in Table 1. The isotherm of C-Fe-16 shows type IV character with an obscure hysteresis loop in the relative pressure range of 0.4–0.55, revealing that partial mesoporosity remained. The pore size distribution (Figure S2, Supporting Information) shows that C-Fe-16 has a small mesopore concentrated at approximately 2.3 nm. Meanwhile, the samples C-Fe-23, C-Fe-45, and C-Fe-50, which have higher Fe_2O_3 loadings, exhibit obvious microporous feature

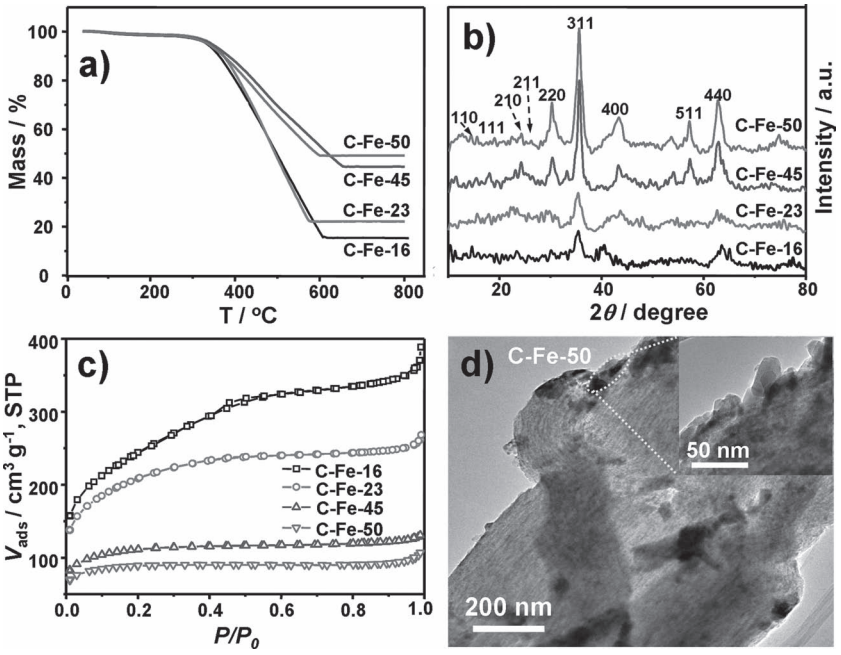

Figure 1. a) TG curves under an air flow, b) wide-angle XRD patterns, and c) N_2 sorption isotherms of the Fe_2O_3@C composites with different Fe_2O_3 loadings. d) Representative TEM image of C-Fe-50 composite (the inset is an HRTEM image of C-Fe-50).

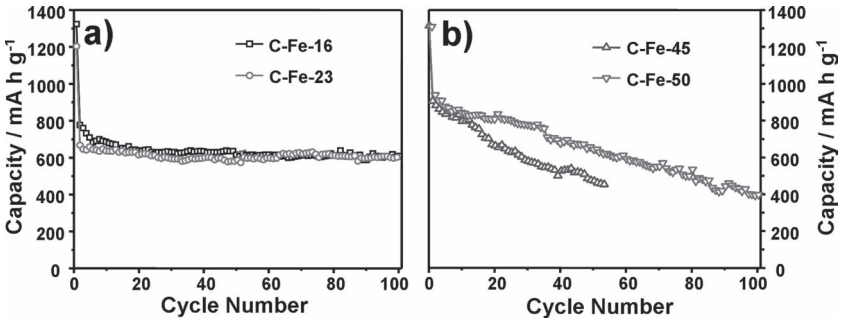

Figure 2. Comparison of cycle performance of the Fe_2O_3@C composites with different Fe_2O_3 loadings. Test conditions: current density of 200 mA g^{-1} between 0.005 and 3 V, taking the total mass of Fe_2O_3@C composites into account.

and much less porosity. The BET surface area of C-Fe-16 is 869 $m^2 g^{-1}$, and is substantially reduced to 737, 385, and 303 $m^2 g^{-1}$ for C-Fe-23, C-Fe-40, and C-Fe-50, respectively. Compared to those (surface area and pore size are 1770 $m^2 g^{-1}$ and 3.0, 5.5 nm) of the native carbon matrix,[32] it is undoubted that the large pore system of carbon were partially filled with Fe_2O_3 crystallites. From TEM images of C-Fe-50 sample (Figure 1d) with 50 wt% Fe_2O_3 loading, it is observed evidently that a part of Fe_2O_3 NPs emerge on the external surface of the carbon matrix.[32,38] This is consistent with the XRD results.

The cycle stabilities of the four samples were evaluated at a current density of 200 mA g^{-1} over a voltage range of 0.005–3 V (**Figure 2**). It is evident that the C-Fe-16 and C-Fe-23 electrodes exhibit much better cycle performance and similar reversible capacities. The reversible capacity of the two samples retained at approximately 600 mA h g^{-1} (based on the total mass of Fe_2O_3@C composites) even after 100 cycles. In order to prove the universality of such composite structure, other transition metal oxides (CoO_x, NiO, and CuO) composites with approximately 22 wt% active materials loading were fabricated and show excellent electrochemical performances (Figure S3, Supporting Information). In contrast, the discharge capacities of C-Fe-45 and C-Fe-50 with a relatively high loading decay dramatically through the entire cycles. Among them, sample C-Fe-45 delivers a relatively low capacity of 455 mA h g^{-1} after 54 cycles, and the reversible capacity of C-Fe-50 is only 400 mA h g^{-1} at the end of 100 cycles. This reduction in capacity is attributed to the following reason: the large contact interface between exposed Fe_2O_3 and electrolyte raises the risk of secondary reactions, including repeating formation and/or decomposition of SEI films during Li^+ insertion/extraction processes due to the expansion/shrinkage of Fe_2O_3 NPs and the catalysis of metallic Fe (Scheme 1). Some previous reports have proved this conclusion in similar transition metal oxides, such as Fe_3O_4 and Cr_2O_3.[20,21] The secondary reactions may cause an extra consumption of Li ion and large irreversible capacity and thus result in a poor cycle performance. Hence, it is urgently necessary to find an effective way of nanoengineering Fe_2O_3@C composites, which not only possess a high tap density and electrochemical capacity, but also show a stable cycle performance. According to the aforementioned studies, reduction of the exposed area of Fe_2O_3 active materials may be a promising approach to improve the cycle stability of the composites. Meanwhile, the higher Fe_2O_3 loading means higher reversible capacity and bulk density; thus the C-Fe-50 sample was selected for further study.

2.3. Nanoengineered Polypyrrole-Coated Fe_2O_3@C Composites for Enhancing Cycle Stability

With the aim of nanoengineering a novel multifunctional composite to avoid direct contact of active materials and electrolyte as well as improving the electronic conductivity, we introduced a thin and conductive PPy layer on the external surface and pore entrances of sample C-Fe-50, and the as-prepared sample was named C-Fe-50-PPy. To confirm the presence of PPy, the sample was characterized by FTIR spectroscopy. The FTIR bands in **Figure 3**a are in good agreement with the results in the literature.[39,40] The band at 1570 cm^{-1} is attributed to the fundamental vibrations of the PPy ring, the one at 1235 cm^{-1} is due to C–N stretching vibrations, at 1045 cm^{-1} to the =C–H in-plane vibrations, and at 925 and 800 cm^{-1} to C–H out-of-plane deformation vibrations of the ring. This indicates the presence of PPy within the Fe_2O_3@C composite. The TG analysis (Figure 3b) shows the C-Fe-50-PPy composite with 47 wt% Fe_2O_3.[41] Considering the original ratio of the components (the weight ratio of Fe_2O_3/C is 1:1) in sample C-Fe-50, the PPy loading is calculated to be approximately 6 wt%.

Figure 4a,b and Figure S4 (Supporting Information) show scanning electron microscopy (SEM) images of the free and PPy-coated Fe_2O_3@C composites. Obviously, after coating PPy on the Fe_2O_3@C composite, the surface appears very smooth. Additionally, the Fe_2O_3@C particles are agglomerated to form a larger unit. PPy is found in bridging the particles, resulting in better contact between particles and facilitating efficient electron transport. TEM was further used to examine the morphology and property of C-Fe-50-PPy composite. As seen in Figure 4c, the Fe_2O_3@C particles are connected together by the PPy layer into a larger unit so that the electron beam can

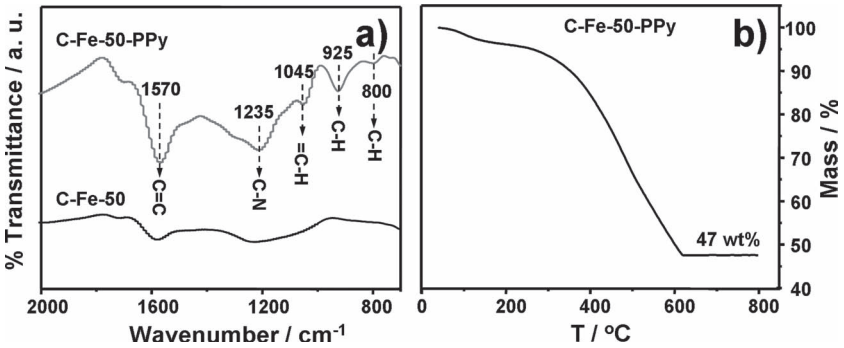

Figure 3. a) FTIR spectra of C-Fe-50-PPy and C-Fe-50. b) TG curve of the C-Fe-50-PPy sample.

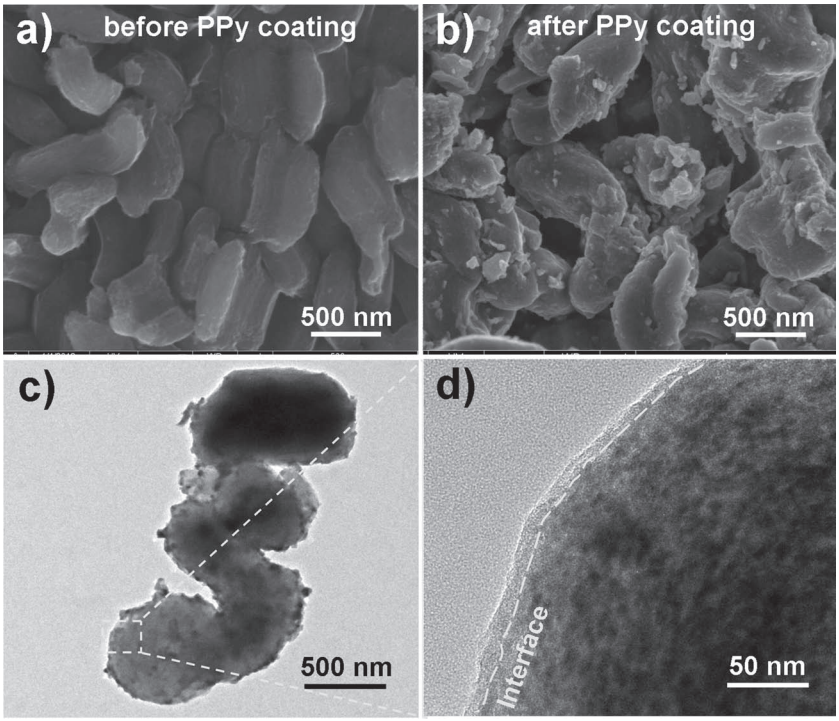

Figure 4. SEM images of Fe_2O_3@C particles before (a) and after (b) PPy coating. In the sample after PPy coating, particles were adhered and wrapped into a larger unit. TEM (c) and HRTEM (d) images of Fe_2O_3@C after PPy coating.

not easily permeate the composite. A high-resolution TEM image (Figure 4d) clearly reveals that the Fe_2O_3@C particles are uniformly and continuously coated by a thin PPy layer with a thickness of 5 to 10 nm, as indicated by the yellow dashed line. Meanwhile, the N_2 sorption isotherm (Figure S5, Supporting Information) shows a remarkable decrease of the nitrogen uptake, indicating the pores are blocked to a great extent. This evidently reveals that the PPy coating layer has been successfully clad on the pore entrances of the carbon matrix; the pore parameters are compiled in Table 1. The tap density of C-Fe-50-PPy composite is measured to be approximately 1.04 g cm^{-3}, which is comparable to commercial graphite materials. To achieve such high tap density for nanostructure materials is still a big challenge.[42–44] On the basis of these results, it is believed that the conductive PPy coating on the Fe_2O_3@C composite is achieved by in situ chemical oxidation polymerization. Such a compact PPy layer could effectively prevent direct contact between the inner active material and solvent, and avoid the formation of an unstable SEI on exposed surfaces of Fe_2O_3. Moreover, the cross-linking of particles could further enhance the electronic conductivity of the composite by reducing the contact resistance among the particles and improve the tap density of composites.

Cyclic voltammetry (CV) was carried out to understand the electrochemical reactive process of this material. **Figure 5**a shows the first four CV curves of C-Fe-50-PPy at room temperature in the range of 0.005–3 V at a scan rate of 0.5 mV s^{-1}. In agreement with literature,[45–47] one pair of distinct redox current peaks can be clearly identified in Figure 5a. The reduction peak at around 0.4 V in the cathodic sweep corresponds to the Li^+ insertion into Fe_2O_3 and the formation of Li_2O and the electrolyte decomposition to form SEI films. On the other hand, the oxidation peak at around 1.8 V in the anodic sweep, attributed to the reversible oxidation from Fe^0 to Fe^{3+}.[45] Apparently, the peak intensity drops significantly in the second cycle, indicating the occurrence of some irreversible reactions with formation of an SEI film.[48] Importantly, the CV curves exhibit a little change from the second to the forth cycle, suggesting a good reversibility of electrochemical reaction.[27,32]

Galvanostatic discharge–charge cycling can provide straightforward evidence about electrochemical properties in reversibility and cyclability. The voltage versus capacity profiles are shown in Figure 5b. A distinct voltage plateau is clearly identified at approximately 0.75 V, agreeing well with the above CV analysis. It can be found that the first discharge and charge capacities are 1164 and 813 mA h g^{-1}, respectively. Surprisingly, the initial coulombic efficiency is high at 70%, which is remarkably higher than those of recent iron oxides and C composite anodes.[49–51] Following the first cycle, the coulombic efficiency

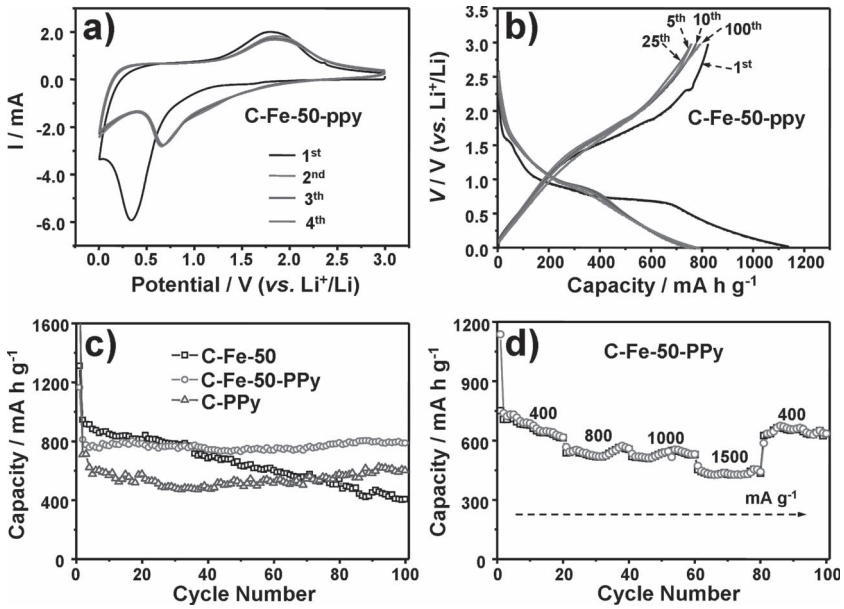

Figure 5. a) Cyclic voltammograms and b) galvanostatic discharge–charge profiles of C-Fe-50-PPy at a current density of 200 mA g^{-1} between 0.005 and 3 V. c) Comparison of the cycle performance, and d) rate capability with increasing current density.

remains high (greater than 97%) and is stable throughout the entire cycle tests, indicating that the formed surface SEI film retains intact and good reversibility of the electrochemical reactions.[32] Obviously, the specific capacities from charge profiles in the 5th, 10th, 25th, and 100th cycle remain nearly unchanged, which is attributed to the compositional and structural stability of the PPy-coated Fe_2O_3@C as anode materials for Li-ion batteries.[49] This result is consistent with the CV analysis.

To highlight the superiority of the unique C-Fe-50-PPy composite for anode materials of LIBs, we tested the cycle performance of the C-Fe-50-PPy composite at a current density of 200 mA g^{-1} on the basis of the total mass of composite. For comparison, C-PPy was also investigated under the same conditions, together with C-Fe-50 as a control. All results are compiled in Figure 5c. It is observed that the capacity of C-Fe-50 fades rapidly to a value lower than 400 mA h g^{-1} after 100 cycles, only 42% capacity retention against at that of the 2nd cycle. Meanwhile, the capacity of C-PPy drops during first several cycles and can remain in a relatively low value of 590 mA h g^{-1} after 100 cycles. In sharp contrast, the C-Fe-50-PPy composite exhibits improved cycle stability and a high reversible specific capacity. A high reversible capacity of 785 mA h g^{-1} is retained over 100 cycles, which corresponds to 97% capacity retention against that at the 2nd cycle. To the best of our knowledge, both the reversible capacity and cycle stability are comparable to the Fe_2O_3@C anodes for LIBs reported so far (see Table S1 for a detailed comparison, Supporting Information). The improved cyclability of C-Fe-50-PPy electrode can be ascribed to the unique multifunctional composite structure (Scheme 1), i.e., the synergistic combination of the thin conductive PPy coating layer and carbon wall as a buffer layer to hold stresses caused by volume change. Meanwhile, the PPy layer can prevent direct contact between Fe_2O_3 NPs and electrolyte, thus facilitating the stability of SEI films formed on the surfaces.[33,34,52] In order to clarify the influence of the hybridization on electrochemical performance of the C-Fe-50-PPy, we calculated the theoretical capacity of the physical mixture of pristine materials (Fe_2O_3 and C-PPy) from the theoretical capacities of the Fe_2O_3 (1007 mA h g^{-1}) and C-PPy (590 mA h g^{-1}), respectively. In view of the contents of Fe_2O_3 and C-PPy, using computational models,[53,54] a theoretical capacity of the C-Fe-50-PPy composite is calculated as follows: $C_{theoretical} = C_{Fe2O3} \times \omega_{Fe2O3} + C_{C\text{-}PPy} \times \omega_{C\text{-}PPy} = 0.47 \times 1007 + 0.53 \times 590 = 786$ mA h g^{-1}. The results show that the C-Fe-50-PPy can deliver a high reversible capacity of 785 mA h g^{-1} that is equal to about 100% of the theoretical capacity. To further increase the thickness of the PPy layer (Figure S6, Supporting Information), the stability of samples was remained, but the reversible capacity decreases, indicating the importance of achieving a thin PPy layer.

Importantly, taking the advantage of the unique nanostructure and the surface selective coated PPy layer, C-Fe-50-PPy composite showed excellent rate capability at continuously variable current densities (Figure 5d). It delivers a rate capacity of ca. 614 mA h g^{-1} when first cycled at 400 mA g^{-1} for 20 cycles, 555 mA h g^{-1} at 800 mA g^{-1}, and 528 mA h g^{-1} at 1000 mA g^{-1}. Even at a high current density of 1500 mA g^{-1}, the specific capacity still retains a value of approximately 430 mA h g^{-1}. Moreover, when the current density returns to the initial 400 mA g^{-1} after 80 cycles, the composite electrode recovers its original capacity (630 mA h g^{-1} at the 100th cycle), which is markedly superior to previously reported Fe_2O_3-based electrodes that suffer from sluggish kinetics.[12,50,55] The results suggest that the structure of C-Fe-50-PPy remains stable even under high rate cycling.

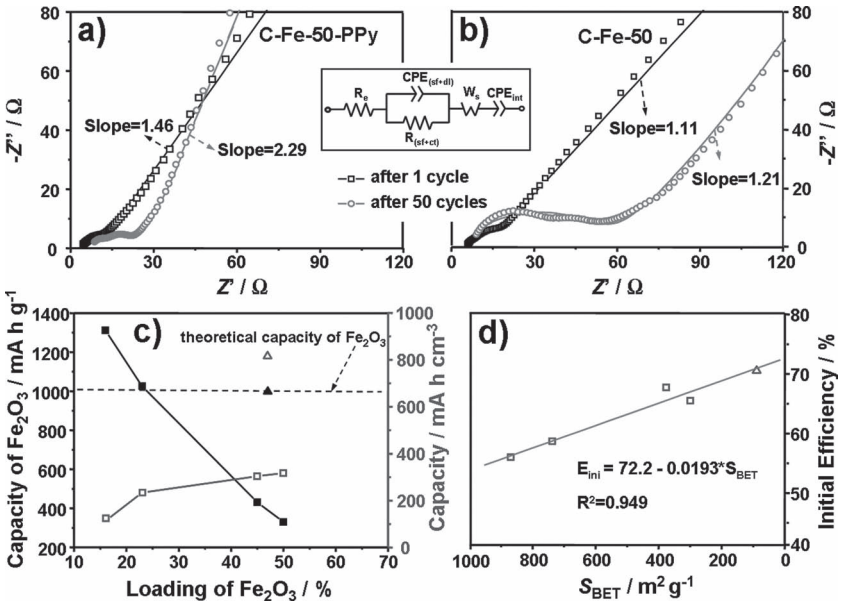

Figure 6. Nyquist plots of C-Fe-50-PPy (a) and C-Fe-50 (b) after 1 cycle (in black squares) and 50 cycles (in red circles). Symbols represent experimental spectra and continuous lines represent fitted data using the equivalent electrical circuit, shown inset. c) Practical capacities of Fe_2O_3 in as-prepared samples (black solid symbols) and volumetric capacity of the as-prepared samples (blue hollow symbols) with different Fe_2O_3 loadings (note: capacity is the discharge capacity after 100 cycles except for that of sample C-Fe-45, which is only 54 cycles.). d) The relationship between S_{BET} and the initial coulombic efficiency (E_{ini}). The squares represent C-Fe-x (x = 16, 23, 45, or 50), and the triangles represent C-Fe-50-PPy sample.

Actually, the high rate capability and the cycle stability are mainly related to the thickness of SEI film, interfacial charge-transfer process, and lithium-ion diffusion in a composite. To gain further insight into the electrochemical performance, electrochemical impedance spectroscopy (EIS) measurements were carried out at room temperature on the cells after the 1st and 50th cycles (**Figure 6**a,b). The Nyquist plots obtained for C-Fe-50-PPy and PPy-free C-Fe-50 composites in the fully delithiation state were collected for comparison. The measured impedance data were analyzed by fitting to an equivalent electrical circuit in Figure 6, inset, similar to the circuit employed for pioneering reported Fe_2O_3,[7] NiO,[56] and metal oxyfluorides materials.[57] The intercept at the real impedance (Z') axis in the high-frequency region corresponds to the ohmic resistance (R_e), which represents the total resistance of the electrolyte, separator and electrical contacts. The diameter of the semicircle in

the middle frequency range indicates the Li^+ migration resistance (R_{sf}) through the SEI film and the charge-transfer resistance (R_{ct}). A constant phase element, $CPE_{(sf+dl)}$, used instead of pure capacitance due to the depressed semicircle observed in the spectra. The inclined line in the lower frequency is related to the Warburg impedance, which is associated with lithium-ion diffusion in the solid. CPE_{int} substitutes for intercalation capacitance. The fitting values from the equivalent circuit are presented in Table S2 (Supporting Information). We mainly focus on the comparison of $R_{(sf+ct)}$ here. No obvious difference of $R_{(sf+ct)}$ between the two samples can be seen after one cycle. However, after 50 cycles, the $R_{(sf+ct)}$ of C-Fe-50-PPy increases slightly from 6.8 to 22.0 Ω, while the one of C-Fe-50 without PPy increased dramatically from 7.3 to 58.6 Ω. This means that both SEI resistance and charge-transfer resistance are significantly reduced after PPy coating. As seen, the low-frequency tail is also different, which is compared qualitatively with the steeper low-frequency tail, indicating higher lithium ion conductivity in the electrode materials.[56] As expected, the PPy coating layer improves the stability of SEI films, the rate of charge-transfer, and Li-ion kinetics for Li insertion and extraction, thus resulting in improved cycle performance and enhanced electrode reaction kinetics during charge/discharge processes.

To highlight the good electrochemical performance of C-Fe-50-PPy, we further compared its practical capacity of Fe_2O_3 in composite and volumetric capacity with that of as-prepared Fe_2O_3@C samples; the results are listed in Table S3 (Supporting Information). As shown in Figure 6c, it is obvious that the practical capacity of Fe_2O_3 in C-Fe composites decreases with increased Fe_2O_3 loading. However, the practical capacity of Fe_2O_3 in C-Fe-50-PPy is 1004 mA h g^{-1}, which is close to the theoretical capacity (1007 mA h g^{-1}) at a high Fe_2O_3 loading (47 wt%). Furthermore, since many nanomaterials have a low packing density, all empty space in the electrode will be flooded by electrolyte, increasing the weight without adding capacity. Moreover, a high capacity should be achieved in some small-scale cell packs, such as mobile phone cells. Therefore, volumetric capacity is more important than the widely used gravimetric one. From Figure 6c, it is also clear that C-Fe-50-PPy multifunctional composite dramatically increase the volumetric capacity to 816 mA h cm^{-3}. The highest value of the other Fe_2O_3@C composites is not more than 320 mA h cm^{-3}. Meanwhile, as a summary, a well-fitted linear relationship between the specific surface area (S_{BET}) and initial coulombic efficiency (E_{ini}) can be obtained by fitting the experimental S_{BET} and E_{ini} (Figure 6d). As expected, the E_{ini} gradually increases as the decrease of S_{BET}, and C-Fe-50-PPy shows the highest initial coulombic efficiency of 70%. These results confirmed that C-Fe-50-PPy possesses simultaneously the highest use efficiency of Fe_2O_3, volumetric capacity and initial coulombic efficiency, which is attributed to the unique multifunctional composite nanostructure. To further prove the important role played by the PPy coating layer in enhancing the electrochemical performance, the spent C-Fe-50-PPy and C-Fe-50 composites were characterized by TEM after 50 cycles (Figure S7, Supporting Information). By comparison, it is evidently demonstrated that the ordered mesostructures of C-Fe-50-PPy remain intact and Fe_2O_3 NPs are immobilized and well-encapsulated in the carbon matrix, indicating that the PPy layer can effectively maintain the structure integrity of Fe_2O_3@C during cycles.

Overall, several factors might have contributed to the excellent electrochemical performance of the C-Fe-50-PPy multifunctional composite anodes. First, the carbon walls provide a confined environment for anchoring and maintaining a high dispersity of Fe_2O_3 NPs during charge/discharge processes. Meanwhile, the adequate void space of the mesopore channels can act as a "buffer zone" for accommodating volume expansion of fine Fe_2O_3 NPs. This has been proved in our previous work.[32] Second, the Fe_2O_3@C composite is homogenously coated with a thin PPy layer to avoid the direct contact interface area between Fe_2O_3 and electrolyte, which effectively reduces the degree of the repeated formation/decomposition of SEI film, thus maintaining good cycle stability. Third, the cross-linking of the Fe_2O_3@C composites bridged by PPy layer enhances the electrical conductivity by reducing the contact resistance, leading to improved cycle performance and rate capability, and the high tap density of the composite. Apparently, the synergistic effect of PPy coating layer and the carbon matrix is the key issue to enhance the stability and rate capability of Fe_2O_3 active materials. A further exploration and development of the hierarchical, multifunctional composite with conductive polymer, Fe_2O_3, and tubular mesoporous carbon would be beneficial to fabricate new composite anodes with desired capacity, high-rate capability, and cycle stability as well as high volumetric capacity.

3. Conclusions

We have designed and assembled a novel multifunctional nanostructure for an electrochemically stable and high efficient Fe_2O_3-based electrode material. The morphological and structural investigations reveal that the PPy was uniformly coated onto the surface of Fe_2O_3@C composites and this unique structure apparently shows optimum electrochemical performance, due to the formation of the protective layer and improvement of electrical conductivity, as compared with PPy-free Fe_2O_3@C composites. By combining such fascinating advantages of nanosized Fe_2O_3 particles, highly porous carbon matrix, and conductive PPy layer, the nanoengineered multifunctional composite is a promising anode material for highly efficient LIBs. Optimistically, this type of multifunctional composite structures could be extended for the fabrication of other cathode and anode electrode materials, to achieve high performance LIBs; work in this direction is underway in our laboratory.

4. Experimental Section

Synthesis of Carbon Matrix and Fe_2O_3@C Composites: Tubular mesoporous carbon was synthesized via a nanocasting approach using SBA-15 template, as described in our previous reports.[58,59] The Fe_2O_3@C composites were prepared via impregnation and direct pyrolysis processes. In a typical procedure, 5 mL $Fe(NO_3)_3 \cdot 9H_2O$ solution with different concentrations (0.94, 1.88 or 2.33 M) were obtained containing 50 μL HCl (37%). Subsequently, the calculated amount of $Fe(NO_3)_3 \cdot 9H_2O$ solution, based on the total pore volume of the carbon matrix, was then impregnated into the pore channels of carbon, and dried at 50 °C for 3 h. Finally, the powder was heated to 400 °C with a heating rate of 2°C min^{-1}

for 4 h under an argon atmosphere. The impregnation and pyrolysis steps were repeated one more time in order to further increase the Fe_2O_3 loading. The as-prepared composites with different Fe_2O_3 loading were denoted as C-Fe-*x* (*x* = 16, 23, 45, 50), where *x* stands for the Fe_2O_3 content, as measured by a thermogravimetric analyses.

Synthesis of Polypyrrole-Coated Fe_2O_3@C Composites: The PPy coating was conducted by vapor-phase polymerization as follows: 0.1 mL of solution composed with 0.3 M $FeCl_3 \cdot 6H_2O$ as the oxidant and 0.033 M *p*-toluenesulfonic acid as the dopant was added into 0.15 g C-Fe-50 matrix under stirring at room temperature. After the solution had been absorbed, the powder was put into a Teflon bottle where a vial containing 2 mL pyrrole monomer was used for generate pyrrole vapor, without direct contact to the powder sample. After sealing, the bottle was left at room temperature for 12 h. Finally, the product was washed and dried at 50 °C, and named as C-Fe-50-PPy. As a control experiment, C-PPy was prepared with similar procedure without impregnation of $Fe(NO_3)_3 \cdot 9H_2O$.

Characterization: Thermogravimetric analysis was measured from 25 to 800 °C in air with a heating rate of 10 °C min^{-1}, using a STA449 F3 Jupiter thermogravimetric analyzer (NETZSCH). The structures of the obtained composites were characterized by X-ray diffraction (XRD) (pert, Philips) using Cu Kα radiation. Nitrogen adsorption was performed with a Micromeritics Tristar 3000 instrument at liquid nitrogen temperature to determine the surface area and porosity. Fourier transform infrared (FTIR) spectra were recorded using a Nicolet iN10 (Thermo scientific Co., Ltd., USA) with KBr pellets. Scanning electron microscopy (SEM) was carried out with a FEI Nova NanoSEM 450 instrument at 10 kV. High-resolution transmission electron microscopy (HRTEM) investigations were performed in a Hitachi HF2000 microscope equipped with a cold field emission gun at a beam energy of 200 kV. Samples were dispersed on a copper mesh. The tap density of the powders was tested as follow: a certain amount of powder was added into a dry measuring cylinder, and then the measuring cylinder was taped until the volume of the powders did not change any longer. The ratio of the mass and the volume was the tap density of the powders.

Electrochemical Characterization: Electrochemical experiments were performed using 2025 coin-type cells. The working electrode consisted of 80 wt% active material, 10 wt% conductive carbon black and 10 wt% commercial LA133 binder (Indigo, China, Essential Component: PAN). The each electrode area was about 1.13 cm^2 and the active mass 2.0–2.5 mg cm^{-2}. The electrolyte was a solution of 1 M $LiPF_6$ in EC/DMC/EMC (1:1:1 by volume). Pure Li foil was used as the reference and counter electrode. Celgard 2400 was used as a separator. The charge/discharge measurements were carried out in the voltage window from 0.005 to 3.0 V using a Land CT2001A battery test system at room temperature. The specific capacity of all as-prepared composites was calculated by using the total mass of Fe_2O_3 and carbon or/and PPy. Cyclic voltammetry (CV) measurements and electrochemical impedance spectra (EIS) were performed on a CHI660D electrochemical workstation.

Supporting Information

Supporting Information is available from the Wiley Online Library or from the author.

Acknowledgements

The project was supported by the Fundamental Research Funds for the Central Universities, the Program for New Century Excellent Talents in University of China (NECT-09-0254), the National Natural Science Foundation of China (NSFC 21103184), and the Ph.D. Programs Foundation (20100041110017) of the Ministry of Education of China.

Received: August 9, 2012
Revised: October 4, 2012
Published online: October 26, 2012

[1] P. G. Bruce, B. Scrosati, J.-M. Tarascon, *Angew. Chem. Int. Ed.* **2008**, *47*, 2930.
[2] H. Li, Z. Wang, L. Chen, X. Huang, *Adv. Mater.* **2009**, *21*, 4593.
[3] J. Cabana, L. Monconduit, D. Larcher, M. R. Palacín, *Adv. Mater.* **2010**, *22*, E170.
[4] F. Cheng, J. Liang, Z. Tao, J. Chen, *Adv. Mater.* **2011**, *23*, 1695.
[5] Y. Liu, D. Liu, Q. Zhang, G. Cao, *J. Mater. Chem.* **2011**, *21*, 9969.
[6] M. M. Thackeray, C. Wolverton, E. D. Isaacs, *Energy Environ. Sci.* **2012**, *5*, 7854.
[7] M. V. Reddy, T. Yu, C.-H. Sow, Z. X. Shen, C. T. Lim, G. V. S. Rao, B. V. R. Chowdari, *Adv. Funct. Mater.* **2007**, *17*, 2792.
[8] C. Ban, Z. Wu, D. T. Gillaspie, L. Chen, Y. Yan, J. L. Blackburn, A. C. Dillon, *Adv. Mater.* **2010**, *22*, E145.
[9] S. Yang, X. Feng, S. Ivanovici, K. Müllen, *Angew. Chem. Int. Ed.* **2010**, *49*, 8408.
[10] X. Wang, Z. Yang, X. Sun, X. Li, D. Wang, P. Wang, D. He, *J. Mater. Chem.* **2011**, *21*, 9988.
[11] D. Larcher, C. Masquelier, D. Bonnin, Y. Chabre, V. Masson, J.-B. Leriche, J.-M. Tarascon, *J. Electrochem. Soc.* **2003**, *150*, A133.
[12] W.-J. Yu, P.-X. Hou, L.-L. Zhang, F. Li, C. Liu, H.-M. Cheng, *Chem. Commun.* **2010**, *46*, 8576.
[13] J. S. Chen, T. Zhu, X. H. Yang, H. G. Yang, X. W. Lou, *J. Am. Chem. Soc.* **2010**, *132*, 13162.
[14] J. Liu, Y. Li, H. Fan, Z. Zhu, J. Jiang, R. Ding, Y. Hu, X. Huang, *Chem. Mater.* **2010**, *22*, 212.
[15] T. Yoon, C. Chae, Y.-K. Sun, X. Zhao, H. H. Kung, J. K. Lee, *J. Mater. Chem.* **2011**, *21*, 17325.
[16] Z. Wang, D. Luan, S. Madhavi, C. M. Li, X. W. Lou, *Chem. Commun.* **2011**, *47*, 8061.
[17] X.-L. Wu, Y.-G. Guo, L.-J. Wan, C.-W. Hu, *J. Phys. Chem. C* **2008**, *112*, 16824.
[18] S. Yuan, Z. Zhou, G. Li, *CrystEngComm* **2011**, *13*, 4709.
[19] P. Balaya, H. Li, L. Kienle, J. Maier, *Adv. Funct. Mater.* **2003**, *13*, 621.
[20] J. Hu, H. Li, X. Huang, L. Chen, *Solid State Ionics* **2006**, *177*, 2791.
[21] W.-M. Zhang, X.-L. Wu, J.-S. Hu, Y.-G. Guo, L.-J. Wan, *Adv. Funct. Mater.* **2008**, *18*, 3941.
[22] B. Koo, H. Xiong, M. D. Slater, V. B. Prakapenka, M. Balasubramanian, P. Podsiadlo, C. S. Johnson, T. Rajh, E. V. Shevchenko, *Nano Lett.* **2012**, *12*, 2429.
[23] H. Liu, X. Du, X. Xing, G. Wang, S. Z. Qiao, *Chem. Commun.* **2012**, *48*, 865.
[24] K. Brezesinski, J. Haetge, J. Wang, S. Mascotto, C. Reitz, A. Rein, S. H. Tolbert, J. Perlich, B. Dunn, T. Brezesinski, *Small* **2011**, *7*, 407.
[25] Y.-G. Guo, J.-S. Hu, L.-J. Wan, *Adv. Mater.* **2008**, *20*, 2878.
[26] E. Kang, Y. S. Jung, A. S. Cavanagh, G.-H. Kim, S. M. George, A. C. Dillon, J. K. Kim, J. Lee, *Adv. Funct. Mater.* **2011**, *21*, 2430.
[27] Y. Song, S. Qin, Y. Zhang, W. Gao, J. Liu, *J. Phys. Chem. C* **2010**, *114*, 21158.
[28] Z. Wang, D. Luan, S. Madhavi, Y. Hu, X. W. Lou, *Energy Environ. Sci.* **2012**, *5*, 5252.
[29] Z. Wu, K Yu, S. Zhang, Y. Xie, *J. Phys. Chem. C* **2008**, *112*, 11307.
[30] M. Nagao, M. Otani, H. Tomita, S. Kanzaki, A. Yamada, R. Kanno, *J. Power Source* **2011**, *196*, 4741.
[31] Y. Zhai, Y. Dou, D. Zhao, P. F. Fulvio, R. T. Mayes, S. Dai, *Adv. Mater.* **2011**, *23*, 4828.
[32] F. Han, W.-C. Li, M.-R. Li, A.-H. Lu, *J. Mater. Chem.* **2012**, *22*, 9645.
[33] Y. Yang, G. Yu, J. J. Cha, H. Wu, M. Vosgueritchian, Y. Yao, Z. Bao, Y. Cui, *ACS Nano* **2011**, *5*, 9187.
[34] G.-C. Li, G.-R. Li, S.-H. Ye, X.-P. Gao, *Adv. Energy Mater.* **2012**, *2*, 1238.
[35] G. Liu, S. Xun, N. Vukmirovic, X. Song, P. Olalde-Velasco, H. Zheng, V. S. Battaglia, L. Wang, W. Yang, *Adv. Mater.* **2011**, *23*, 4679.
[36] L. Nyholm, G. Nyström, A. Mihranyan, M. Strømme, *Adv. Mater.* **2011**, *23*, 3751.

[37] A.-H. Lu, J.-J. Nitz, M. Comotti, C. Weidenthaler, K. Schlichte, C. W. Lehmann, O. Terasaki, F. Schüth, *J. Am. Chem. Soc.* **2010**, *132*, 14152.
[38] Z. Wu, W. Li, P. A. Webley, D. Zhao, *Adv. Mater.* **2012**, *24*, 485.
[39] M. Omastová, M. Trchová, J. Kovářová, J. Stejskal, *Synth. Met.* **2003**, *138*, 447.
[40] Y. Fu, A. Manthiram, *J. Phys. Chem. C* **2012**, *116*, 8910.
[41] X. Liang, Z. Wen, Y. Liu, H. Zhang, J. Jin, M. Wu, X. Wu, *J. Power Sources* **2012**, *206*, 409.
[42] G. Wang, H. Liu, J. Liu, S. Qiao, G. M. Lu, P. Munroe, H. Ahn, *Adv. Mater.* **2010**, *22*, 4944.
[43] G. Jeong, Y.-U. Kim, H. Kim, Y.-J. Kim, H.-J. Sohn, *Energy Environ. Sci.* **2011**, *4*, 1986.
[44] B. Guo, X. Wang, P. F. Fulvio, M. Chi, S. M. Mahurin, X.-G. Sun, S. Dai, *Adv. Mater.* **2011**, *23*, 4661.
[45] B. Wang, J. S. Chen, H. B. Wu, Z. Wang, X. W. Lou, *J. Am. Chem. Soc.* **2011**, *133*, 17146.
[46] Y. NuLi, P. Zhang, Z. Guo, H. Liu, *J. Electrochem. Soc.* **2008**, *155*, A196.
[47] C. T. Cherian, J. Sundaramurthy, M. Kalaivani, P. Ragupathy, P. S. Kumar, V. Tgavasi, M. V. Reddy, C. H. Sow, S. G. Mhaisalkar, S. Ramakrishna, B. V. R. Chowdari, *J. Mater. Chem.* **2012**, *22*, 12198.
[48] B. Sun, J. Horvat, H. S. Kim, W.-S. Kim, J. Ahn, G. Wang, *J. Phys. Chem. C* **2010**, *114*, 18753.
[49] W.-J. Yu, P.-X. Hou, F. Li, C. Liu, *J. Mater. Chem.* **2012**, *22*, 13756.
[50] L. Ji, O. Toprakci, M. Alcoutlabi, Y. Yao, Y. Li, S. Zhang, B. Guo, Z. Lin, X. Zhang, *ACS Appl. Mater. Interfaces* **2012**, *4*, 2672.
[51] S. M. Yuan, J. X. Li, L. T. Yang, L. W. Su, L. Liu, Z. Zhou, *ACS Appl. Mater. Interfaces* **2011**, *3*, 705.
[52] R. Liang, H. Cao, D. Qian, J. Zhang, M. Qu, *J. Mater. Chem.* **2011**, *21*, 17654.
[53] S.-M. Paek, E. Yoo, I. Honma, *Nano Lett.* **2009**, *9*, 72.
[54] Y. Luo, J. Luo, J. Jiang, W. Zhou, H. Yang, X. Qi, H. Zhang, H. J. Fan, D. Y. W. Yu, C. M. Li, T. Yu, *Energy Environ. Sci.* **2012**, *5*, 6559.
[55] Y. Ma, G. Ji, J. Y. Lee, *J. Mater. Chem.* **2011**, *21*, 13009.
[56] G. Zhou, D.-W. Wang, L.-C. Yin, N. Li, F. Li, H.-M. Cheng, *ACS Nano* **2012**, *6*, 3214.
[57] M. V. Reddy, S. Madhavi, G. V. S. Rao, B. V. R. Chowdari, *J. Power Sources* **2006**, *162*, 1312.
[58] A.-H. Lu, W. Schmidt, B. Spliethoff, F. Schüth, *Adv. Mater.* **2003**, *15*, 1602.
[59] A.-H. Lu, W.-C. Li, W. Schmidt, W. Kiefer, F. Schüth, *Carbon* **2004**, *42*, 2939.